Eichhorn et al. *EPJ Techniques and Instrumentation* (2022) 9:2
https://doi.org/10.1140/epjti/s40485-022-00077-y
EPJ.org
EPJ Techniques and Instrumentation
RESEARCH ARTICLE
Open Access

Single- and two-photon absorption laser-induced fluorescence spectroscopy in rare gases for gridded ion thruster diagnostics

Christoph Eichhorn[1*], Lukas Pietzonka[1], Frank Scholze[1], Carsten Bundesmann[1], Daniel Spemann[1], Horst Neumann[1] and Hans J. Leiter[2]

*Correspondence:
christoph.eichhorn@iom-leipzig.de
[1]Leibniz Institute of Surface Engineering (IOM), Permoserstrasse 15, 04318, Leipzig, Germany
Full list of author information is available at the end of the article

Abstract

Methods based on laser-induced fluorescence spectroscopy are widely used for spatially resolved non-intrusive diagnostics of atomic or molecular densities and velocity distributions in plasma applications. With regard to electric space propulsion, one focus is on the investigation of rare gases such as xenon or krypton, which are currently the favored propellants in gridded ion- and Hall-effect thrusters. For gridded ion engines, diagnostics of neutral atoms is of interest since charge-exchange processes between neutrals and ions are the main driver of accelerator grid erosion, which limits the lifetime of a gridded ion thruster. Extending the capabilities of the advanced electric propulsion diagnostics platform which has been developed by the IOM and partners, single- and two-photon absorption laser-induced fluorescence diagnostics have been set-up recently at our institute. Both experimental set-ups, and as a series of first applications, measurements of krypton neutrals in the plume of the radiofrequency ion thruster RIT-10 (ArianeGroup GmbH), and xenon neutrals within the discharge chamber of a gridded radiofrequency ion source developed at IOM, are presented.

Keywords: Laser-induced fluorescence; Two-photon absorption laser-induced fluorescence; Electric propulsion diagnostics; Neutral atom diagnostics

1 Introduction

Laser-induced fluorescence has been widely established for non-intrusive diagnostics of atom or molecular species in non-thermal equilibrium plasmas, such as direct current, high-frequency, microwave or helicon discharges, among many further applications [1–5].

Frequently, laser-induced fluorescence is used as general term for several techniques that require further differentiation. Their common principle is the state-selective excitation of an atomic or molecular energy level by absorption of continuous or pulsed laser radiation, while detecting the subsequent fluorescence resulting from radiative de-excitation of the excited level(s). For plasma diagnostic purposes, most commonly, single-photon absorption laser-induced fluorescence (henceforth LIF) and two-photon absorption laser-

induced fluorescence (henceforth TALIF) have been employed. In both cases, the particle excitation kinetics may be described with rate equation models (see e.g. [6, 7]), which give access to the measurement of plasma parameters of interest, for example, the relation between the detected signal intensity and the particle density of the probed state. Other related techniques use multi-photon absorption (i. e. three photons or more) [8], or two-photon absorption laser-induced stimulated emission [9], which are here only mentioned as further method examples based on laser-induced fluorescence.

The question whether LIF or TALIF should be applied, essentially depends on the plasma parameter to be measured and the plasma species to be investigated. If, for example, the neutral density of an atomic plasma species is of interest, laser-induced excitation from the atomic ground state is advantageous: Then, even though the population density distribution in a non-Boltzmann equilibrium plasma remains unknown, the ground state density can be identified with the particle density, since in many low temperature plasmas ground state depletion may be neglected.

Ground state excitation, for some atomic species like neutral titanium or molybdenum, is achievable within the wavelength range of commercially available, frequency-doubled dye lasers via LIF [10–13]. Other species of interest, however, such as atomic hydrogen, oxygen, nitrogen, and also rare gas atoms like neutral xenon or krypton would require laser wavelengths in the VUV. In order to circumvent such short excitation wavelengths, which would result in significantly more complex set-ups including Raman-shifted lasers [14, 15], simultaneous absorption of two photons can be applied. Examples of TALIF spectroscopy for plasma diagnostics are the determination of particle densities of low-Z atoms in plasma flows or jets [16–22], whereas measurements in rare gases, such as on neutral xenon or krypton, have been reported significantly less frequently, with concentration on the investigation of the neutral density depletion in helicon plasmas [23–25] or on a microwave cathode [26].

Furthermore, LIF is used to investigate plasma quantities that can be measured independently of the knowledge of excited state population densities, such as neutral or ion temperatures, or their velocity distributions. In such applications, the shape and the spectral (Doppler-)shift of the absorption line is analyzed. Without the necessity for probing the ground state, laser-induced transitions, for example from a lower metastable state, can be performed at wavelengths in the VIS or NIR ranges, which allows for the use of narrow-band tunable diode lasers in many applications [27–30].

The scope of this article focusses on LIF and TALIF diagnostics of rare gas-driven gridded ion sources, as they are used for terrestrial applications such as surface engineering or etching [31], and beyond, as ion thrusters for electric space propulsion. At present, gridded ion engines play an increasingly important role in commercial and scientific spacecraft mission design, besides Hall-effect or stationary plasma thrusters, which use gridless particle acceleration within an annular ceramic discharge channel, as another major group [32]. The operational lifetime of gridded ion thrusters significantly depends on grid erosion, especially of the accelerator grid, a process that is mainly driven by slow secondary ions produced in charge exchange process between thermal neutrals and fast primary ions accelerated within the grid system [33, 34]. Since the accelerator grid usually gets negatively biased in order to suppress electron backflow into the discharge chamber, these slow secondary ions may get re-attracted by the accelerator grid and sputter the grid surface, resulting e.g. in a widening of the grid holes. Apart from the near-grid area, the charge

exchange plasma in the plume of an ion- or Hall-effect thruster may interact with other parts of the spacecraft, such as solar arrays, which is also subject of numerical modelling [35–37].

As ion thruster lifetime testing up to several tens of thousands operation hours is technically and financially costly, several numerical codes related to grid erosion and lifetime prediction have been established [38–42]. At IOM, the 2D grid erosion code DYNASIM is used, based on an in-house developed module computing the neutral flow throughout a series of hole apertures, and the commercially available ion trajectory code IGUN [43, 44]. This code has been validated [45] for selected operation conditions of RIT-22 thruster (ArianeGroup GmbH). The application of LIF of TALIF diagnostics as described in the following is motivated to address two major needs of such codes: (1) The measurement of input parameters, such as the ion and neutral velocity distribution (temperature) within the discharge chamber, and (2) the verification of numerical models of the neutral gas flow and the plume expansion throughout the ion optic system, based on the spatially resolved measurement of neutral particle densities. Both velocity distributions and particle densities may considerably affect numerically calculated grid erosion rates.

In this paper, progress on the use of laser-induced fluorescence spectroscopy for electric space propulsion diagnostics is reported. Results of a first series of measurements in the plume of the radiofrequency ion thruster RIT-10 (provided by ArianeGroup GmbH) are presented, extending a recent demonstration of TALIF in neutral krypton on the same thruster [46]. So far, only a very small number of TALIF investigations on gridded ion thrusters in xenon [47, 48] and one for a Hall-effect thruster [49] exist. In addition, LIF and TALIF are demonstrated inside the discharge chamber of a gridded rf ion source. Very few LIF measurements in the discharge chamber of gridded ion sources focussing on discharge cathode and erosion-related phenomena have been reported [50, 51], along with extensive investigations of velocity distributions in the plume and the discharge near the exit plane of Hall-effect thrusters [5, 52–64].

The work presented here has been carried out in order to extend the diagnostic capabilities of the Advanced Electric Propulsion Diagnostics (AEPD) platform, which has been set up by IOM and partners [65–67]. The platform has been applied for thruster characterization in several measurement campaigns and involves measurement sensors for monitoring mechanical parts such as grid temperature (pyrometer, thermocamera) and grid/channel erosion (telemicroscope, triangular laser head). For beam diagnostics a Faraday probe, a retarding potential analyzer, an $E \times B$ probe (contributed by Aerospazio Tecnologie, Rapolano Terme, Italy) [68, 69] and an active thermal probe (contributed by Christian-Albrechts-Universität zu Kiel, Kiel, Germany) [70, 71] are available. We mention this here to underline that the design of the LIF and TALIF set-ups, such as the vacuum-sided LIF probe, is compatible to be implemented on this system or can be used in parallel. With both diagnostics ready to use with the platform, implementation has proceeded so far that they can be applied in measurement campaigns on advanced thruster characterization.

2 Description of the experimental methods and set-ups

Measurements as described in the following have been carried out using two ion sources: (1) A RIT-10, provided by ArianeGroup GmbH, which is a radiofrequency ion thruster

including a two-grid screen-accelerator system [72, 73]. Operated with xenon as standard, krypton has been used here to demonstrate that TALIF spectroscopy is applicable in the plume for future detailed analysis of this thruster including this propellant. (2) The radiofrequency ion source ISQ40RF, which has been developed at IOM [74] and includes a three-grid screen-accelerator-deccelerator system. The discharge chamber wall of this source consists of UV fused silica, giving optical access for measurements within the chamber.

During all experiments, the vacuum facility at IOM with 3 m in length and 1.1 m in diameter has been used. Three motorized linear stages are available inside the chamber to move the ion source with respect to the measurement position of interest. The facility is evacuated using two serial combinations of multi-stage roots pumps and turbo pumps (pumping speeds 1000 l/min and 2000 l/s, respectively), and one cryo pump (8000 l/s), reaching a base pressure of some 10^{-7} mbar.

2.1 Two-photon absorption laser-induced fluorescence (TALIF)

The TALIF process is based on the laser-induced simultaneous absorption of two photons, and the detection of the subsequent fluorescence of the excited level. The transition rate W for the absorption process is provided by perturbation theory in quantum mechanics, which allows deriving the formalism to calculate the two-photon absorption cross sections and the relation between transition rate and laser intensity. One finds for an n-photon absorption process $W = \hat{\sigma}^{(n)} I^n$ [75]. If calculated, using the respective n-photon absorption cross section $\hat{\sigma}^{(n)}$ and practicable laser intensities I, theses rates decrease by several orders of magnitude with every order in n, reducing likewise the fluorescence signal intensities to be detected. Considering TALIF transitions, the two absorbed photons may differ in color or polarization, and follow the two-photon electric dipole selection rules [76]. In many applications, as also here, nanosecond pulsed dye lasers are used to generate the required laser power densities for the absorption of two photons of same wavelength and polarization, but also picosecond-TALIF has been demonstrated in plasma diagnostics [22].

The population densities of the involved levels (the excited level and usually the ground state) are commonly modelled in a set of coupled rate equations, which has been extensively described in literature [7, 77]. Its solution yields the relation between the TALIF signal intensity and the ground state density n_0 [7]

$$S = D \frac{E^2}{a^2} \frac{A_{21}}{A+Q} \frac{\hat{\sigma}^{(2)} n_0}{4\pi^2 (\hbar\omega)^2} \int_{-\infty}^{\infty} F^2(t)\, dt. \tag{1}$$

Herein E is the energy of the laser pulse, a the beam waist at the detection area, ω and $F(t)$ are the frequency and the temporal profile of the laser pulse, respectively. A_{21} is the transition rate for the selected fluorescence channel, $A = \tau^{-1} = \sum_i A_{2i}$ the inverse natural lifetime of the upper level, Q the quenching rate and $\hat{\sigma}^{(2)}$ the two-photon absorption cross section. Assuming a Gaussian temporal laser profile $F(t)$, the integral is $\int F^2(t)\, dt = (\sqrt{\pi}\tau_p)^{-1}$, wherein τ_p is the FWHM duration of the laser pulse. The calibration constant D includes all relevant efficiencies and gains related to the detection apparatus, as well as geometric factors and the detection solid angle. If D is kept unchanged during an experiment, the measurement of relative ground densities is straightforward. In order to calibrate the TALIF signal intensity to absolute densities, measurements at well-defined reference con-

ditions can be applied, circumventing the need for the determination of the calibration constant [78].

A major challenge in the present application is the low TALIF signal intensity, resulting from the small neutral particle densities in the plume of an ion engine (typically in the range of $10^{17} - 10^{18}$ m^{-3}), and the small detection solid angle when the detection optics have to be placed outside a large-scaled vacuum chamber, or at least in practicable distance to the thruster. Increasing the laser power density at the detection volume in order to improve signal intensities, however, needs to proceed with caution, since processes competing to TALIF such as resonant multi-photon ionization may not longer be negligible, and saturate the TALIF signal. In this case, $S \propto E^2$ does not hold, and the rate equations need to be complemented with terms for photoionization [7], significantly complicating the derivation of particle densities. Since, here, the $S \propto E^2$ relation is difficult to be checked accurately due to above-mentioned restrictions, in the present approach $S \propto n_0$, is verified for a fixed laser pulse energy in a separate experiment within the range of the expected neutral densities. Measurements in the plume or in the discharge chamber are carried out using the same laser pulse energy.

The experimental set-up is unchanged as described earlier [46, 79]: Pulsed tunable laser radiation is generated using a dye laser (LPD3000, Lambda Physics) pumped by a Nd:YAG laser (Surelite III, Continuum). The output (pulse duration 4.5 ns) is frequency-doubled using appropriate beta barium borate crystals, producing wavelengths at approximately 212.6 nm (excitation of the $5p[1/2]_0$ level in krypton) and approximately 222.6 nm (excitation of the $6p'[1/2]_0$ level in xenon). The step width in spectral scans is 0.5 pm. The used laser dyes are Stilbene-3 (krypton) and Coumarin 120 (xenon). The estimated laser linewidth is 0.15 cm^{-1}, which is assumed to be large compared to the expected line splitting due to isotope shift for both two-photon transitions applied in xenon and krypton. Note that hyperfine splitting does not occur since the total electronic angular momentum is $J = 0$ for the ground states and the two-photon excited levels, respectively. The beam is focussed from outside of the vacuum chamber to the region of interest, using a lens with a focal length of $f = 75$ cm. A small fraction of the beam is diverted to monitor the laser pulse energy using a pyroelectric energy meter (ES111C, Thorlabs).

The fluorescence is detected perpendicular to both the direction of the laser beam propagation and the central thruster axis. A $f/2$ lens is used to image the detection volume on the entrance slit of a gated photomultiplier (R758-10, Hamamatsu). Optical bandpass filters are used to separate the fluorescence channel of interest, for krypton at $\lambda = 758.7$ nm (filter center wavelength: 760 nm, bandwidth: 19 nm) and for xenon at $\lambda = 788.7$ nm (filter center wavelength: 788 nm, bandwidth: 8 nm). The photomultiplier output is integrated using a boxcar averager (SR250, Stanford Research Systems), plasma background emission using a second boxcar, and a integration gate delay of 500 ns. The boxcar output is processed using a computer interface (SRS245, Stanford Research Systems), the time-resolved fluorescence is analyzed with an oscilloscope with a bandwidth of 1.5 GHz and a maximum sample rate of 4 GS/s (CobraMax, Gagescope). A low jitter delay generator (DG645, Stanford Research Systems) is used to set all required temporal trigger pulses. Data acquisition is controlled using a LabView program. The schematics of the set-up is displayed in Fig. 1 and the implementation in Fig. 2.

Figure 3 displays the TALIF schemes applied in neutral krypton and neutral xenon. In order to check the reliability of the set-up, the lifetimes of the excited states have been

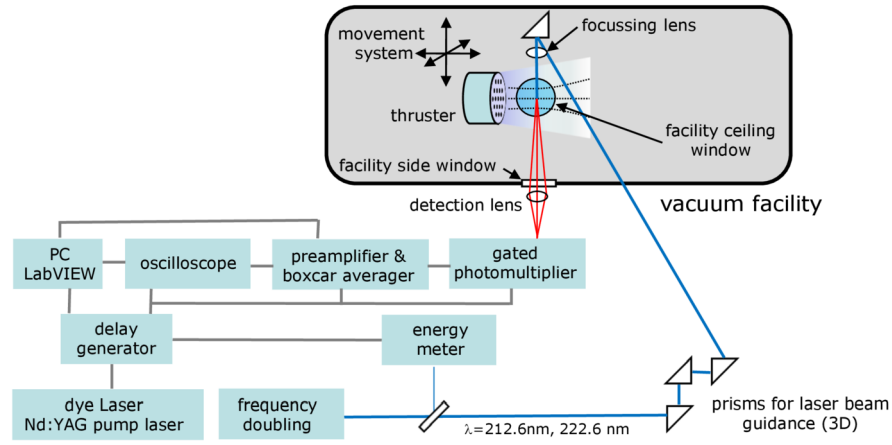

Figure 1 Schematics of the TALIF set-up for ion thruster diagnostics

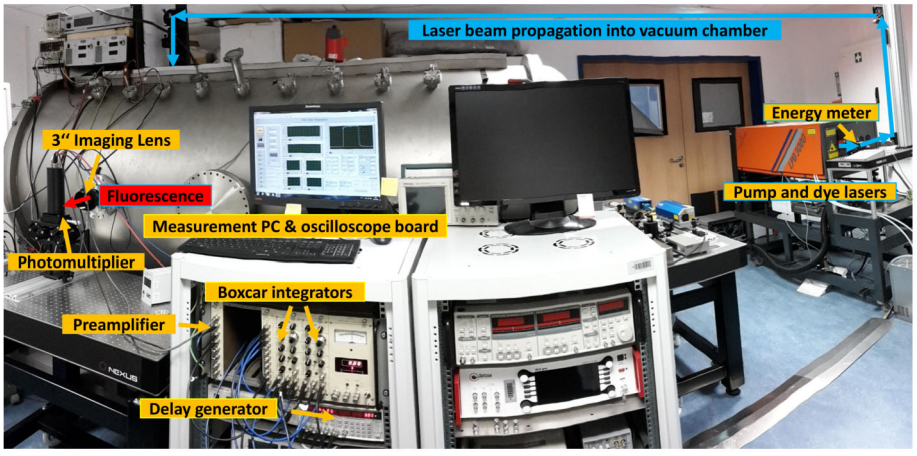

Figure 2 TALIF set-up for ion thruster diagnostics as realized in the lab at IOM. Image modified from Eichhorn et al. Paper IEPC-2019-503 [79]

measured for both levels in the thruster plume. For the krypton $5p[1/2]_0$ level, a lifetime $\tau = 26$ ns has been found [46], and for the xenon $6p'[1/2]_0$ level $\tau = 41$ ns [80]. Both are in reasonable agreement with literature values of the natural lifetimes for these levels [81, 82], respectively. Collisional deactivation is negligible at the small neutral particle densities in the plume mentioned above.

2.2 Single-photon absorption laser-induced fluorescence (LIF)

Different from the TALIF approach, probing rare gas species with LIF, as discussed in the following, uses excitation of visible or near-infrared transitions arising from lower excited states populated by collisions in the plasma. Since those transitions are accessible through tunable narrow-linewidth continuous-wave (cw) lasers, LIF spectroscopy allows for species-sensitive and spatially resolved measurement of spectral absorption lineshapes, with negligible contributions from laser-linewidth broadening. The laser wavelength is tuned across the range of interest and the absorption spectrum gets mapped by synchronously monitoring the fluorescence collected from the detection volume. For

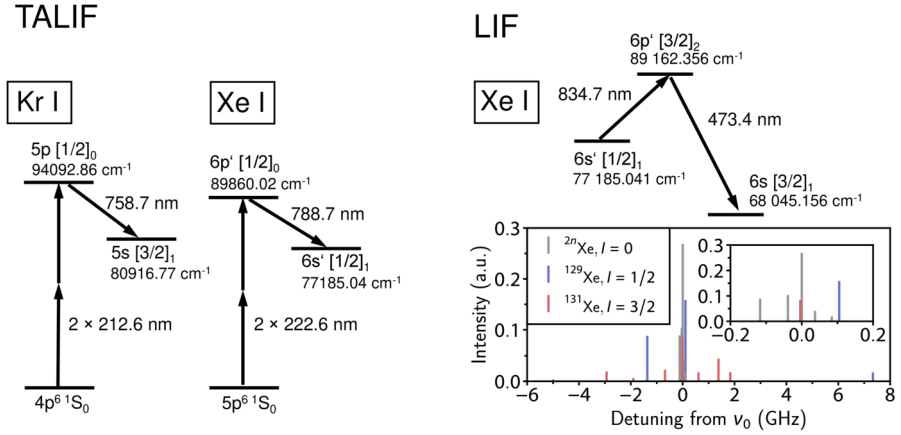

Figure 3 Excitation schemes used in the present work. Left: TALIF schemes in neutral krypton and neutral xenon. Right: LIF scheme in neutral xenon (top), spectral positions (line broadening excluded) of the hyperfine structure lines (bottom)

the LIF investigation of xenon neutrals reported here, the transition scheme shown in Fig. 3(right, top) has been applied.

In the non-saturated regime, the fluorescence signal S scales linearly with the laser intensity I_{ex}, and directly reflects the spectral lineshape ψ of the absorption cross-section [53]:

$$S(\nu - \nu_0) \propto I_{\mathrm{ex}} \psi(\nu - \nu_0). \tag{2}$$

Above a characteristic, so-called, saturation intensity, the fluorescence intensity becomes non-linear and grows asymptotically with increasing I_{ex}, as the rate at which atoms in the lower state absorb laser photons, approaches or exceeds the relaxation rate of the upper state. Since the saturation intensity intrinsically depends on the spectral lineshape of the absorption cross-section, a LIF spectrum recorded within the saturated regime shows a laser intensity dependent broadening, often referred to as power broadening [52, 83].

The absorption cross-section lineshape is the convolution of three contributing parts, $\psi = \psi_{\mathrm{n}} * \psi_{\mathrm{d}} * \psi_{\mathrm{hfs}}$ [54, 63]: (1) Natural broadening, which follows a Lorentzian profile ψ_{n}. (2) Doppler broadening: Given an atom of the probed species moving with non-vanishing speed u along the axis defined by the laser beam, its absorption frequency as seen from the laboratory frame, is shifted from its resonance frequency at rest, ν_0, by $\nu_{\mathrm{d}} = -\nu_0 u/c$. Then, the velocity distribution function of the species projected onto the laser beam axis, $f(u)$, directly translates into a distribution of laboratory-frame absorption frequencies,

$$\psi_{\mathrm{d}}(\nu - \nu_0) = \frac{c}{\nu_0} f\left[\left(1 - \frac{\nu}{\nu_0}\right)c\right]. \tag{3}$$

(3) The hyperfine structure lineshape function ψ_{hfs} originating from nine stable or long-living isotopes, respectively, see Fig. 3(right, bottom): The variance in nuclear mass and volume results in individually shifted transition lines with their intensities weighted according to the isotope abundance distribution. The components related to isotopes with non-vanishing nuclear spin are subject to further splitting due to the interaction between

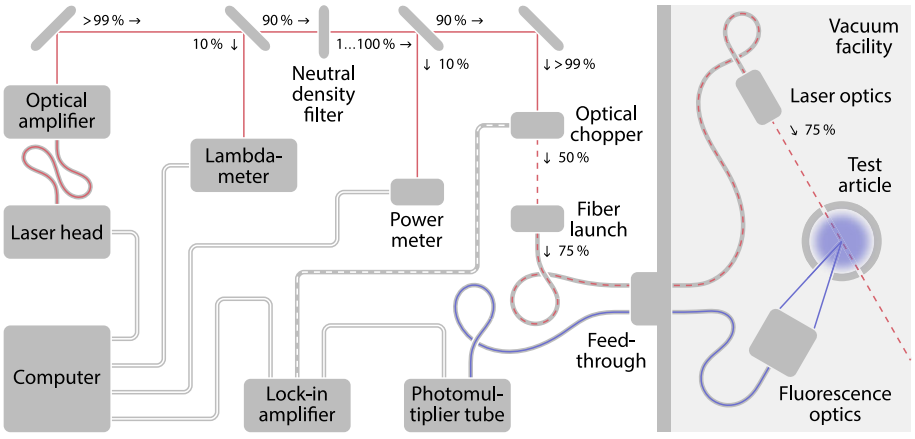

Figure 4 Schematics of the LIF setup. Optical transmissions or reflectances of each element placed in the laser beam path are denoted, optical fibers are visualized by curved lines

nuclear magnetic and electric moments with the fields generated by the orbital electrons. The hyperfine structure is computed on the basis of tabulated isotope data and nuclear-spin splitting interaction constants from [84], details regarding the reconstruction of the hyperfine structure lineshape function can be found in [54, 85].

The experimental set-up for LIF spectroscopy can be sectioned into three parts: the laser system with accompanying diagnostics, the vacuum-sided LIF optics, and the LIF signal acquisition unit. Figure 4 shows the LIF set-up schematically.

The cw laser system is implemented following the MOPA (master-oscillator power-amplifier) scheme: A narrow-linewidth extended-cavity diode laser (DL pro, Toptica) with Littrow design seeds a semiconductor optical amplifier (BoosTA, Toptica) with plano-tapered active layer waveguide geometry. The seed laser wavelength can be selected between approximately 800 and 840 nm. Performing a voltage ramp on the piezoelectric actuator attached to the grating enables quasi-continuous laser wavelength tuning within a few picometers, by regulating the diode injection current in proportion to the actuator voltage, a mode-hop-free tuning range up to 32 GHz is reached at 835 nm. The nominal laser linewidth is 200 kHz.

A fraction of approximately 10% of the power of primary beam is used for characterization of the laser output. A high-precision self-calibrating lambdameter (WS7-60 UV-I, HighFinesse) containing a rigid assembly of five Fizeau interferometers is used for measurement of the laser wavelength. The absolute accuracy is 60 MHz, the measurement resolution is 10 MHz. Since the laser diode injection current varies upon wavelength scanning, laser power monitoring is mandatory for subsequent correction of the LIF signal intensity. Here, a digitally controlled photodiode power sensor (PM100D and S120C, Thorlabs) is used.

The main beam passes a chopper wheel (SR540, Stanford Research Systems) which provides the reference signal by two internal optical switches. The chopping frequency is approximately 960 Hz. The beam is coupled into a single-mode optical fiber by means of a commercial optical fiber launch (PAF2A-A15B, Thorlabs). Using a vacuum feedthrough compatible with FC/APC fiber patch cord connectors, the laser beam is guided to the respective optical probe inside the vacuum facility.

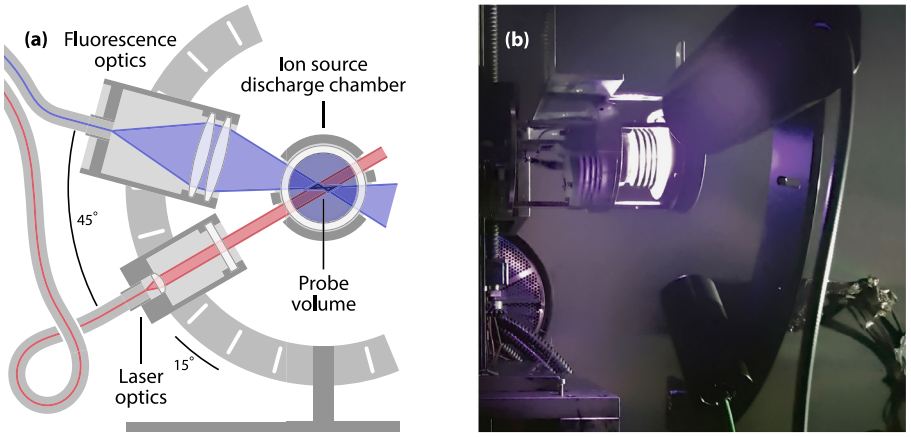

Figure 5 (**a**) Schematics of the LIF vacuum optics arrangement (not to scale). The effective viewing angles of the optical probes are restricted due to supporting elements of the ion source; the intermediate angle between laser propagation and detection axis was set to 45 degrees for optimum laser insertion and fluorescence detection. (**b**) Ion source discharge chamber and the LIF vacuum setup in side view

The probe optics for fiber decoupling consists of a tiltable fixed-focus collimation unit that provides a parallel laser beam with 2 mm in diameter, which determines the minimum width of the probe volume, and thus the lower limit for spatial resolution. The collimator is protected with an anti-reflection coated window. Fluorescence collection optics uses two biconvex lenses, which image the detection volume on the aperture of a multi-mode optical fiber patch cord whose entrance connector can be adjusted with respect to three degrees of freedom.

A semi-circular mounting with an inner diameter of 200 mm (larger mountings available) allows for variable placement of both the laser and the fluorescence optics within a common plane determined by the optical axes intersecting at the probe volume (see Fig. 5). For the experiments presented in the following, the plane defined by the laser and detection directions has been arranged perpendicular to the center axis of the ion source. In that way, the radial velocity component of the investigated plasma species in the discharge chamber can be measured by aligning the laser beam and the fluorescence detection cone with one of the gaps between the turns of the ion source rf coil. Here, the probe volume is located on the cylindrical discharge vessel centerline approximately 20 mm upstream the screen grid.

The fluorescence signal is detected using a fiber-coupled photomultiplier assembly (R7518, Hamamatsu), equipped with an optical band-pass filter to select the fluorescence channel of interest at $\lambda = 473.4$ nm. The photomultiplier output is integrated using a digital lock-in amplifier (SR830, Stanford Research Systems). Typical integration times varied from 300 ms to 3 s for each wavelength step depending on the selected laser power and the fluorescence intensity level. Data acquisition along with synchronized laser wavelength tuning is performed via a LabVIEW interface.

3 Results and discussion

3.1 TALIF in the plume of the RIT-10 thruster

First, the linearity of the TALIF signal intensity with the neutral density was checked as a basic requirement that quantitative analysis of relative and absolute neutral densities

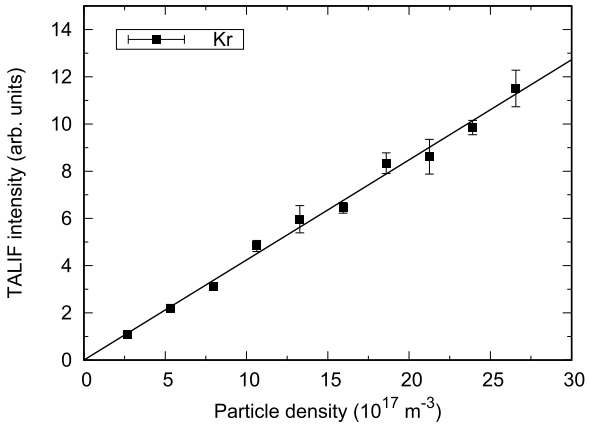

Figure 6 TALIF signal measured for krypton background densities in the vacuum facility, measured during cold gas flow operation at a distance appropriately aside the thruster axis

is possible for the given experimental parameters. The laser pulse energy is fixed, and remains unchanged in all following measurements. The detection volume is slightly defocussed with respect to the focal point of the laser beam focussing lens, which also is kept constant henceforth. The measurement position was sufficiently far off the central axis of the thruster, so that the TALIF signal can be assumed to reflect the background neutral density in the vacuum facility, which was varied with the cold gas flow through the thruster.

Figure 6 shows the TALIF signal intensity plotted over the estimated krypton density at the measurement position. Each data point corresponds to a full scan of the absorption profile, accumulating typically 1500 laser pulses at each wavelength step. The laser pulse repetition frequency is 10 Hz. Full absorption profile scanning, although costly in terms of measurement time, has been maintained in all experiments, with exception of the radial profile shown in Fig. 8. The time-resolved fluorescence is recorded for every laser pulse, with examples of spectral profiles and the fluorescence decay shown in [46]. Figure 6 verifies that the TALIF signal is linear over the range of expected neutral krypton densities in the plume.

The densities given on the abscissa in Fig. 6, however, deserve some attention. As it is common for the background pressure, the density needs to be calculated from a pressure measurement, which faces considerable uncertainties with respect to absolute numbers at pressure ranges of about 10^{-5} mbar or below. Including gas correction needed for using hot cathode gauges, uncertainties accumulate to at least 20 – 30%, as already mentioned in [46]. It is emphasized that this problem affects calibration to absolute densities, while relative changes may be regarded as much more accurate. This is not a serious drawback here, since the interest in these first experiments concentrates on relative density measurements, and a procedure for the absolute calibration circumventing the need for pressure measurements at such low ranges is currently under investigation.

Figure 7 shows axial profiles of the neutral density in the plume of the RIT-10 measured for operation with krypton. Measurement positions are on the central thruster axis. The thruster was operated at 8 sccm at a beam current of 210 mA. These parameters have been selected as a test case for the TALIF approach, rather than a thruster operating condition, which is commonly operated with xenon at some lower mass flows and higher mass

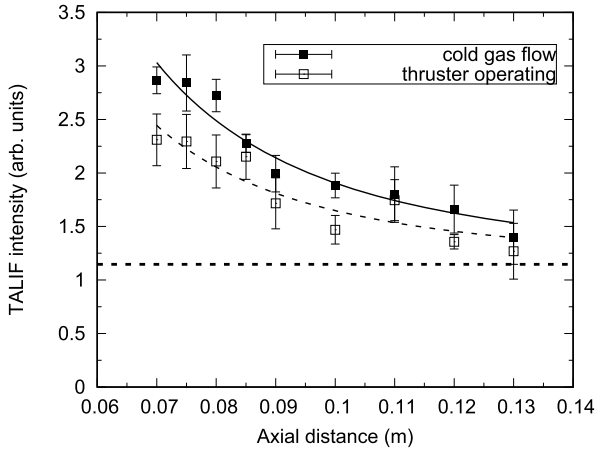

Figure 7 Axial profiles of the krypton neutral densities on the central thruster axis. The distances are given to the accelerator grid on the center axis

utilization efficiencies. Here, measurements under thruster operation and in the cold gas flow have been recorded consecutively, turning off the ion extraction for the cold gas flow. Since the width of the absorption profile is dominated by the linewidth of the dye laser, variations in the Doppler width resulting from variations in the temperature of the detected neutral krypton atoms are so small over the expected temperature range that they are regarded as negligible.

The krypton background density in the vacuum facility (dashed straight line in Fig. 7) has been estimated from the averaged TALIF signal ratios for each axial measurement position and the mass utilization efficiency calculated for the operating condition above. As it can be seen, the contribution of the background density to the TALIF signals is still significant in our vacuum facility, at least at the investigated axial measurement distances. This might be improved by a higher pumping speed in the future. Obviously, the correction of the TALIF signal for the background density becomes more accurate for measurement positions closer to the accelerator grid. However, the present limitation is due to the RIT-10 itself: Since the thruster housing protrudes over the plane defined by the accelerator grid on the central thruster axis by approximately 6 cm, and laser beam and detection directions were perpendicular the thruster axis, no measurement positions closer than 7 cm were possible in the current set-up. Alternative experimental geometries, as worked out currently, shall overcome such spatial restrictions.

The result of a radial scan at an axial distance of 8 cm is shown in Fig. 8. The measurement has been conducted in the cold gas flow at 12 sccm of krypton, which is approximately twice the mass flow that is typical for a RIT-10, but may be taken as a starting point for neutral gas expansion analysis. Here, instead of recording a full spectral scan of the absorption profile for every radial position, the laser wavelength was set fixed to the absorption maximum in a spectral scan performed directly before the radial scan started. Then, the fluorescence of 1500 laser pulses has been accumulated for every radial position. Care has been taken to check that no instrumental drift affects the signal intensities by repeating the measurement at the initial radial position after the radial scan was completed.

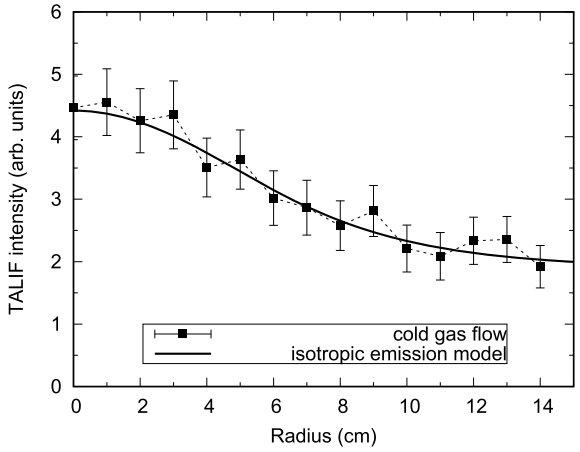

Figure 8 Radial profile of the krypton density at the axial distance of 8 cm. Adopted from Eichhorn et al. Paper IEPC-2019-503 [79]

As expected, the TALIF intensity drops from the center towards outer radial positions, and approaches asymptotically the intensity of the background density in the facility. In Fig. 8, the shape of the radial distribution is compared to an analytic isotropic gas expansion model [48, 86]

$$n_0 \propto \left(1 - \frac{(\frac{r}{R})^2 + (\frac{d}{R})^2 - 1}{\sqrt{[1 + (\frac{r}{R})^2 + (\frac{d}{R})^2]^2 - 4(\frac{r}{R})^2}}\right) \tag{4}$$

wherein d is the distance to the accelerator plane, R the grid extraction radius, and r the radial coordinate.

Although the shape of the profiles seem to be in good agreement, it cannot be expected that Eq. (4) yields a comprehensive model of the neutral gas expansion, since the more detailed thruster geometry such as the aforementioned protrusion of the housing, or the grid curvature are not included. No attempt has been made so far to compare the axial and radial data to the model mentioned above, or to a more sophisticated consistent model of neutral gas expansion, since an extensive number of axial and radial profiles are required, including in particular the area close to the accelerator grid, which is, however, content of ongoing work.

Figure 9 displays the dependency of the TALIF intensity on the beam current for thruster operation at a krypton flow of 7 sccm. The measurement position was at an axial distance of 8 cm on the central thruster axis. As expected, the signal drops with increasing beam current, reflecting the increasing mass utilization efficiency. Extrapolating the data to the equivalent current of the mass flow, the background TALIF intensity is found to be in reasonable agreement to the previous measurements.

3.2 TALIF and LIF in the discharge chamber of an ion source

Another step in non-intrusive diagnostics development is aiming at the application of LIF and TALIF inside the discharge chamber of an ion thruster. Here, the neutral densities of xenon or krypton are larger than in the plume, however, the resulting TALIF signal gain goes along with significantly stronger plasma emission that may considerably perturb the

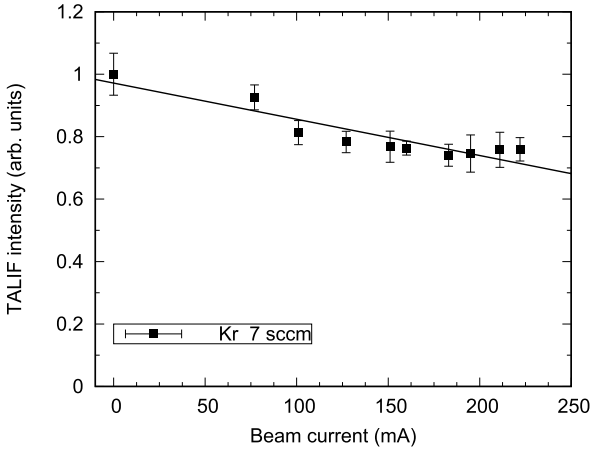

Figure 9 TALIF signal intensity depending on the beam current at fixed mass flow, as a measure for the mass utilization efficiency

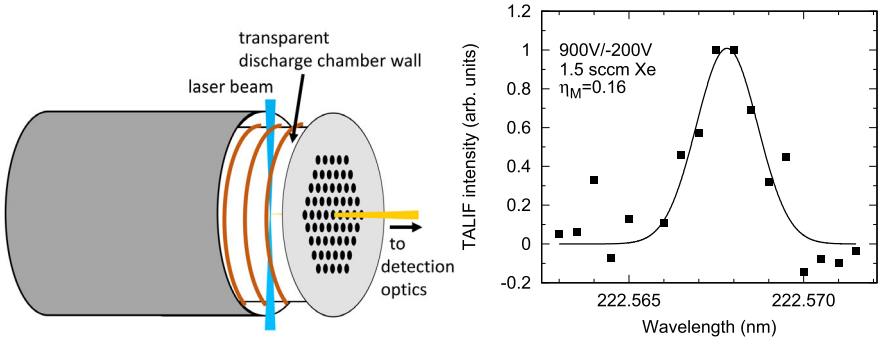

Figure 10 Left: Directions of excitation and fluorescence detection in a TALIF approach inside the discharge chamber of an ion source. Right: TALIF profile in the discharge chamber for the indicated operation condition

measured absorption profiles. For non-ground state LIF, the situation is different, since excited low-energy levels populated by collisions within the discharge are the key element of any excitation scheme. In either case, optical access at least in the direction of laser propagation must be available. Since this would require significant modifications to an ion thruster, first measurements have been carried out on the IOM-developed gridded ion source ISQ40RF [74], which is equipped with an UV fused silica discharge chamber wall, providing sufficient space that the laser beam can propagate into the chamber between the coil windings.

In a first approach, TALIF signals in neutral xenon were detected through the grid holes in the direction of the ion source axis (Fig. 10, left), circumventing a second path for detection through the discharge chamber wall. The measurement position was approximately 1 cm upstream of the screen grid, the ion source was located approximately 40 cm from the window of the vacuum facility. The position of the center grid hole with respect to the detection axis was optimized in the cold gas flow, in which also the linearity of the TALIF signal with the mass flow was checked.

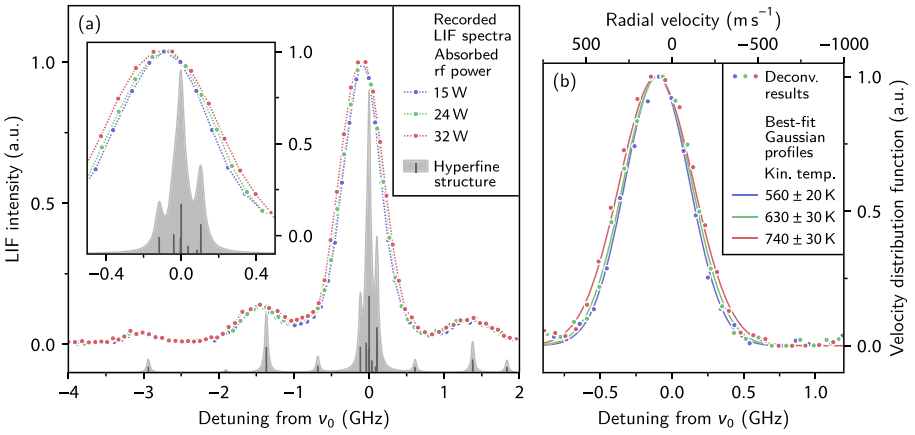

Figure 11 (**a**) Xenon LIF spectra of the transition at 834.7 nm measured in the center of the ion source discharge chamber for three different operation conditions (normalization to maximum LIF intensity; dotted lines are guides to the eyes). The computed naturally broadened hyperfine structure lineshape has been drawn with a vertical offset for clarity. The inset shows the line center with a stretched frequency detuning axis. (**b**) Doppler lineshapes (projected radial velocity distribution functions, respectively) extracted from the LIF spectra (circle markers) and best-fit Gaussian profiles (solid lines) depending on the respective kinetic temperature of the xenon neutrals

When the ion source was turned on, strong emission from the plasma was detected, depending on the rf power. The fluorescence was isolated at the transition at 788.7 nm, minimizing line blending of the most prominent xenon emission lines using the bandpass filter. However, TALIF signals have been acquired under discharge conditions, with an example shown in Fig. 10 (right). Signals were detectable for mass efficiencies up to 20-25%, above that limit the background emission perturbed the TALIF signal too strongly for analysis. Since it is obvious that neutral particle densities at operating conditions at higher mass utilization efficiencies are of interest, forthcoming experiments concentrate on improving the signal-to-noise ratio, including the set-up of another detection direction.

Unlike the TALIF measurements, LIF signals from the discharge chamber have been detected in radial direction through the UV fused silica vessel. The velocity component in parallel to the radially injected laser beam has been examined. Figure 11(a) shows LIF spectra recorded for three operating conditions with different rf powers supplied to the discharge. The measurements were conducted with the laser intensity reduced to the greatest possible extend (approximately 4 mW net laser power). In that way, the LIF intensity was large enough to keep noise at an acceptable level while power broadening of the LIF spectra was suppressed almost completely. Thus, the normalized LIF spectrum is assumed to coincide widely with the spectral lineshape of the absorption cross-section.

Since the lower state of the transition at 834.7 nm is resonantly coupled to the ground state, resonance broadening might occur. In fact, preliminary testing of the LIF setup by replacing the ion source with a commercial xenon spectral calibration lamp (Model 6033, Newport/Oriel Instruments) revealed that resonance broadening is the dominating spectral feature of the lamp within the respective pressure regime. Using the same calibration lamp model, Svarnas et al. observed a spectral line broadening of the same kind [63]. Cedolin et al. investigated resonance broadening in conjunction with a similar xenon transition at 828.0 nm [87]. However, for the ion source examined here with a gas pressure in the discharge chamber in the order of 10^{-3} mbar, the corresponding resonance broaden-

ing width amounts to a few tens of kHz which is well below the expected Doppler width of several hundreds of MHz, or even the natural linewidth of about 50 MHz. Therefore, resonance broadening and further collisional-induced broadening (which should be even weaker) may be neglected when probing xenon neutrals in the ion source discharge chamber. Moreover, potential spectral broadening resulting from Zeeman splitting or the Stark effect can be ruled out on account of the absence of strong magnetic or electric fields at the location of the LIF probe volume.

To extract velocity distribution functions from the measured LIF spectra, the hyperfine structure of the transition lineshape along with natural broadening was eliminated using Fourier deconvolution as proposed in [88]. The convolution of the absorption lineshape constituents is equivalent to multiplication of their Fourier transforms. Therefore, any LIF spectrum (measured in the non-saturated regime) may be reduced to the Doppler-induced lineshape profile by dividing the Fourier transforms of the normalized LIF spectrum and the modeled hyperfine structure including natural broadening. Instead of reconstructing the entire absorption lineshape at once and adjusting it to the measured LIF spectra by curve-fitting methods, the Fourier deconvolution approach directly yields the (projected) velocity distribution function and does not require a-priori modeling of its actual shape.

Embedding additional filters helps to reduce noise induced by discrete sampling in Fourier space. Here, a filter window of boxcar-type was adjusted to each dataset individually to prevent the deconvolution results from filter broadening artifacts. Applying Eq. (3), the Doppler lineshapes obtained this way can be converted to the projected radial velocity distribution function of the xenon neutrals for either ion source operating condition, see Fig. 11(b).

The extracted Doppler lineshapes are well approximated by a Gaussian profile function,

$$\psi'_{\mathrm{d}}(\nu-\nu_0) = A\exp\left[-4\ln(2)\left(\frac{\nu-\nu_0-\Delta\nu_{\mathrm{d}}}{\delta\nu_{\mathrm{d}}}\right)^2\right], \tag{5}$$

indicating that the radial velocity component follows a one-dimensional Maxwellian distribution. Assuming the xenon neutrals are not subject to radial drift, the Doppler shift $\Delta\nu_{\mathrm{d}}$ measured with radial laser injection must vanish. However, a curve-fitting analysis yields finite Doppler shifts of approximately −100 MHz for each of the selected operation conditions. While this would correspond to xenon neutrals preferentially moving away from the laser source at an average speed of about 85 m/s, the observed LIF spectrum redshifts rather result from an systematic error concerning the laser wavelength monitoring. This might result from suboptimal illumination of the Fizeau interferometer assembly within the lambdameter due to coupling with a multimode optical fiber, and hence, a reduction of the absolute accuracy of the read-out wavelength in conjunction with the interferogram calculations handled by the device, which will be improved using a single-mode fiber coupling in future measurements. Further issues that may introduce systematic shifts of the monitored laser wavelength, such as a time delay between incrementing the laser head piezo voltage and the laser wavelength read out as well as improper choice of the laser wavelength sweep rate in comparison to a given lock-in integration time, have been carefully studied in advance and their occurrence has been prevented via appropriate design of the set-up control interface.

As it has been illustrated in Fig. 11, the LIF spectrum and the underlying Doppler lineshape show increasing broadening along with increasing absorbed rf power. Due to equiv-

alence between a Gaussian Doppler lineshape and a Maxwellian velocity distribution function, the Doppler FWHM is directly connected with the kinetic temperature T:

$$\delta\nu_\mathrm{d} = \frac{\nu_0}{c}\sqrt{8\ln(2)\frac{k_\mathrm{b}T}{m}}. \tag{6}$$

With m set to the average atomic weight of xenon of 131.29 u [89], the kinetic temperature of the xenon neutrals is inferred to increase from 560 to 740 K within the tested range of rf powers.

4 Conclusion

TALIF and LIF spectroscopy has been carried out on gridded ion sources. TALIF measurements in neutral krypton are demonstrated in the plume of the gridded ion thruster RIT-10. First results show that axial and radial mapping of the neutral density can be worked out with the newly installed set-up. Although only results for krypton have been shown here, also neutral xenon can be investigated, for which similar signal-to-noise ratios in some parallel experiments at standard thruster operation conditions were found.

As part of a future fully-extended mapping of neutral densities, the need to extend measurements to the near-field directly behind the accelerator grid, or ideally to the inter-grid spacing will be addressed in current modifications of the experimental geometry. This is important as neutral densities significantly contribute to grid erosion via charge exchange processes. Measurement positions close to the exit plane will also allow for direct comparison with numerically computed neutral densities using the IOM-developed erosion code DYNASIM. The effort goes along with the implementation of an improved dye laser system.

In addition, TALIF and LIF measurements inside the discharge chamber of a gridded ion source have been presented. First LIF measurements provided reasonable results of the neutral xenon temperature. Both techniques are demonstrated to be applicable for future measurements on a thruster with appropriate modifications for optical access. The newly set up LIF probe is compatible to be mounted on the AEPD system, and both diagnostics are intended to be used as part of the AEPD system in future ion thruster measurement campaigns.

Acknowledgements
The authors thank R. Woyciechowsky and M. Müller and the workshop at IOM for technical support. ArianeGroup is greatfully acknowledged for providing the RIT-10 thruster. The authors gratefully acknowledge support C. Dankert and A. Neumann from the Deutsches Zentrum für Luft- und Raumfahrt (DLR), Göttingen, Germany, for the loan of a dye laser system used within the present work.

Funding
Work of C. Eichhorn (TALIF) was funded by the Deutsche Forschungsgemeinschaft DFG through grant EI978/1-1. Parts of the work (LIF) was funded by the Deutsches Zentrum für Luft-und Raumfahrt (DLR) through grant BMWi 50RS1506 (Bundesministerium für Wirtschaft und Energie). Both grants are greatfully acknowledged. Open Access funding enabled and organized by Projekt DEAL.

Availability of data and materials
The data sets used and/or analyzed during the current study are available from the corresponding author on reasonable request.

Declarations

Ethics approval and consent to participate
Not applicable.

Consent for publication
All authors agree to the pulication of the article.

Competing interests
The authors declare that they have no competing interests.

Authors' contributions
CE realized the TALIF set-up and parts of the LIF set-up, conducted the TALIF experiments, the data analysis and wrote the main part of the manuscript. LP improved the LIF set-up, performed the LIF measurements and data analysis and wrote the manuscript parts related to LIF. FS extensively supported the operation of the RIT-10 thruster and the ISQ40RF ion source at IOM. HL provided the RIT-10 thruster and supported the operation from ArianeGroup. CB, DS and HN gave genuine and essential support in the project initiation and oversaw the activities. All authors contributed to data interpretation and discussion. All authors read and approved the final manuscript.

Author details
[1]Leibniz Institute of Surface Engineering (IOM), Permoserstrasse 15, 04318, Leipzig, Germany. [2]ArianeGroup GmbH, Postbox 1119, 74239, Lampoldshausen, Germany.

Publisher's Note

Received: 16 December 2021 Accepted: 22 February 2022 Published online: 07 March 2022

References

1. Amorim J, Baravian G, Jolly J. Laser-induced resonance fluorescence as a diagnostic technique in non-thermal equilibrium plasmas. J Phys D, Appl Phys. 2000;33(9):R51–65. https://doi.org/10.1088/0022-3727/33/9/201.
2. Eckbreth AC. Laser diagnostics for combustion temperature and species. 2nd ed. New York: Taylor & Francis; 1996.
3. Skiff F, Bollinger J. Mini-conference on laser-induced fluorescence in plasmas. Phys Plasmas. 2004;11(5):2972–5. https://doi.org/10.1063/1.1668287.
4. Döbele HF, Mosbach T, Niemi K, Schulz-von der Gathen V. Laser-induced fluorescence measurements of absolute atomic densities: concepts and limitations. Plasma Sources Sci Technol. 2005;14(2):S31–41. https://doi.org/10.1088/0963-0252/14/2/s05.
5. Mazouffre S. Laser-induced fluorescence diagnostics of the cross-field discharge of Hall thrusters. Plasma Sources Sci Technol. 2013;22(1):013001. https://doi.org/10.1088/0963-0252/22/1/013001.
6. Lucht RP. Applications of laser-induced fluorescence spectroscopy for combustion and plasma diagnostics. In: Radziemski LJ, Solarz RW, Paisner JA, editors. Laser spectroscopy and its applications. New York: CRC Press; 1987. p. 623–76. https://doi.org/10.1201/9780203749104-9.
7. Bamford DJ, Jusinski LE, Bischel WK. Absolute two-photon absorption and three-photon ionization cross sections for atomic oxygen. Phys Rev A. 1986;34(1):185–98. https://doi.org/10.1103/PhysRevA.34.185.
8. Faisal FHM, Wallenstein R, Zacharias H. Three-photon excitation of xenon and carbon monoxide. Phys Rev Lett. 1977;39(18):1138–41. https://doi.org/10.1103/PhysRevLett.39.1138.
9. Goldsmith JEM. Two-photon-excited stimulated emission from atomic hydrogen in flames. J Opt Soc Am B. 1989;6(11):1979–85. https://doi.org/10.1364/JOSAB.6.001979.
10. Britun N, Gaillard M, Han JG. Laser induced fluorescence for Ti and Ti^+ density characterization in a magnetron discharge. J Phys D, Appl Phys. 2008;41(18):185201. https://doi.org/10.1088/0022-3727/41/18/185201.
11. Britun N, Palmucci M, Konstantinidis S, Snyders R. Particle visualization in high-power impulse magnetron sputtering. I. 2D density mapping. J Appl Phys. 2015;117(16):163302. https://doi.org/10.1063/1.4919006.
12. Gaeta CJ, Turley RS, Matossian JN, Beattie JR, Williamson WS. Plasma erosion rate diagnostics using laser-induced fluorescence. Rev Sci Instrum. 1992;63(5):3090–5. https://doi.org/10.1063/1.1142559.
13. Crofton MW, Patterson MJ. Molybdenum LIF and NEXT erosion rate. In: 34th international electric propulsion conference. Paper IEPC-2015-221. 2015.
14. Döbele HF, Hörl M, Röwekamp M, Reimann B. Detection of atomic oxygen by laser-induced fluorescence spectroscopy at 130 nm. Appl Phys B. 1986;39(2):91–5. https://doi.org/10.1007/BF00694803.
15. Bogen P, Mertens P, Pasch E, Döbele HF. Detection of atomic oxygen and hydrogen in the vacuum UV using a frequency-doubled, Raman-shifted dye laser. J Opt Soc Am B. 1992;9(12):2137–41. https://doi.org/10.1364/JOSAB.9.002137.
16. Fletcher DG. Arcjet flow properties determined from laser-induced fluorescence of atomic nitrogen. Appl Opt. 1999;38(9):1850–8. https://doi.org/10.1364/AO.38.001850.
17. Mazouffre S, Bakker I, Vankan P, Engeln R, Schram DC. Two-photon laser induced fluorescence spectroscopy performed on free nitrogen plasma jets. Plasma Sources Sci Technol. 2002;11(4):439–47. https://doi.org/10.1088/0963-0252/11/4/311.
18. Niemi K, Schulz-von der Gathen V, Döbele HF. Absolute atomic oxygen density measurements by two-photon absorption laser-induced fluorescence spectroscopy in an RF-excited atmospheric pressure plasma jet. Plasma Sources Sci Technol. 2005;14(2):375–86. https://doi.org/10.1088/0963-0252/14/2/021.
19. Löhle S, Eichhorn C, Steinbeck A, Lein S, Herdrich G, Röser H-P, Auweter-Kurtz M. Oxygen plasma flow properties deduced from laser-induced fluorescence and probe measurements. Appl Opt. 2008;47(11):1837–45. https://doi.org/10.1364/AO.47.001837.
20. Marynowski T, Löhle S, Fasoulas S. Two-photon absorption laser-induced fluorescence investigation of CO2 plasmas for Mars entry. J Thermophys Heat Transf. 2014;28(3):394–400. https://doi.org/10.2514/1.T4223.
21. Ceglia G, Del Vecchio A, Koch U, Esser B, Guelhan A. Two-photon laser-induced fluorescence measurements of atomic oxygen density in hypersonic plasma flow. J Thermophys Heat Transf. 2019;33(2):292–9. https://doi.org/10.2514/1.T5354.

22. Klose S-J, Ellis J, Riedel F, Schröter S, Niemi K, Semenov IL, Weltmann K-D, Gans T, O'Connell D, van Helden JH. The spatial distribution of hydrogen and oxygen atoms in a cold atmospheric pressure plasma jet. Plasma Sources Sci Technol. 2020;29(12):125018. https://doi.org/10.1088/1361-6595/abcc4f.
23. Aanesland A, Liard L, Leray G, Jolly J, Chabert P. Direct measurements of neutral density depletion by two-photon absorption laser-induced fluorescence spectroscopy. Appl Phys Lett. 2007;91(12):121502. https://doi.org/10.1063/1.2786601.
24. Magee RM, Galante ME, Gulbrandsen N, McCarren DW, Scime EE. Direct measurements of the ionization profile in krypton helicon plasmas. Phys Plasmas. 2012;19(12):123506. https://doi.org/10.1063/1.4772060.
25. Galante ME, Magee RM, Scime EE. Two photon absorption laser induced fluorescence measurements of neutral density in a helicon plasma. Phys Plasmas. 2014;21(5):055704. https://doi.org/10.1063/1.4873900.
26. Yamashita Y, Tsukizaki R, Kinefuchi K, Koda D, Tani Y, Nishiyama K. Neutral ground state particle density measurement of xenon plasma in microwave cathode by two-photon laser-induced fluorescence spectroscopy. Vacuum. 2019;168:108846. https://doi.org/10.1016/j.vacuum.2019.108846.
27. Severn GD, Edrich DA, McWilliams R. Argon ion laser-induced fluorescence with diode lasers. Rev Sci Instrum. 1998;69(1):10–5. https://doi.org/10.1063/1.1148472.
28. Severn G, Lee D, Hershkowitz N. Xenon ion laser-induced fluorescence using a visible tunable diode laser near 680nm. Rev Sci Instrum. 2007;78(11):116105. https://doi.org/10.1063/1.2813880.
29. Lee D, Hershkowitz N, Severn GD. Measurements of Ar^+ and Xe^+ velocities near the sheath boundary of Ar-Xe plasma using two diode lasers. Appl Phys Lett. 2007;91(4):041505. https://doi.org/10.1063/1.2760149.
30. Chakraborty Thakur S, McCarren D, Lee T, Fedorczak N, Manz P, Scime EE, Tynan GR, Xu M. Laser induced fluorescence measurements of ion velocity and temperature of drift turbulence driven sheared plasma flow in a linear helicon plasma device. Phys Plasmas. 2012;19(8):082102. https://doi.org/10.1063/1.4742178.
31. Frost F, Ziberi B, Schindler A, Rauschenbach B. Surface engineering with ion beams: from self-organized nanostructures to ultra-smooth surfaces. Appl Phys A. 2008;91(4):551–9. https://doi.org/10.1007/s00339-008-4516-0.
32. Holste K, Dietz P, Scharmann S, Keil K, Henning T, Zschätzsch D, Reitemeyer M, Nauschütt B, Kiefer F, Kunze F, Zorn J, Heiliger C, Joshi N, Probst U, Thüringer R, Volkmar C, Packan D, Peterschmitt S, Brinkmann K-T, Zaunick H-G, Thoma MH, Kretschmer M, Leiter HJ, Schippers S, Hannemann K, Klar PJ. Ion thrusters for electric propulsion: scientific issues developing a niche technology into a game changer. Rev Sci Instrum. 2020;91(6):061101. https://doi.org/10.1063/5.0010134.
33. Polk JE, Brophy JR, Wang J. Spatial and temporal distribution of ion engine accelerator grid erosion. In: 31st AIAA/ASME/SAE/ASEE joint propulsion conference and exhibit. AIAA paper 95-2924. 1995. http://hdl.handle.net/2014/30731.
34. Miller JS, Pullins SH, Levandier DJ, Chiu Y-H, Dressler RA. Xenon charge exchange cross sections for electrostatic thruster models. J Appl Phys. 2002;91(3):984–91. https://doi.org/10.1063/1.1426246.
35. Samanta Roy RI, Hastings DE, Gatsonis NA. Numerical study of spacecraft contamination and interactions by ion-thruster effluents. J Spacecr Rockets. 1996;33(4):535–42. https://doi.org/10.2514/3.26796.
36. Wang J, Brinza D, Young M. Three-dimensional particle simulations of ion propulsion plasma environment for deep space 1. J Spacecr Rockets. 2001;38(3):433–40. https://doi.org/10.2514/2.3702.
37. Mikellides I, Jongeward GA, Katz I, Manzella DH. Plume modeling of stationary plasma thrusters and interactions with the express-a spacecraft. J Spacecr Rockets. 2002;39(6):894–903. https://doi.org/10.2514/2.3896.
38. Emhoff JW, Boyd ID. NEXT ion optics modeling of total thruster performance. In: 41st AIAA/ASME/SAE/ASEE joint propulsion conference and exhibit. AIAA paper 2005-3687. 2005. https://doi.org/10.2514/6.2005-3687.
39. Wirz RE, Anderson JR, Katz I. Time-dependent erosion of ion optics. J Propuls Power. 2012;27(1):211–7. https://doi.org/10.2514/1.46845.
40. Wang J, Polk J, Brophy J, Katz I. Three-dimensional particle simulations of ion-optics plasma flow and grid erosion. J Propuls Power. 2003;19(6):1192–9. https://doi.org/10.2514/2.6939.
41. Anderson JJ, Katz I, Goebel D. Numerical simulation of two-grid ion optics using a 3D code. In: 40th AIAA/ASME/SAE/ASEE joint propulsion conference and exhibit. AIAA paper 2004-3782. 2004. https://doi.org/10.2514/6.2004-3782.
42. Nakano M. Three-dimensional simulations of grid erosion in ion engines. Vacuum. 2003;83(1):82–5. https://doi.org/10.1016/j.vacuum.2008.03.080.
43. Becker R, Herrmannsfeldt WB. IGUN - a program for the simulation of positive ion extraction including magnetic fields. Rev Sci Instrum. 1992;63(4):2756–8. https://doi.org/10.1063/1.1142795.
44. Tartz M, Hartmann E, Deltschew R, Neumann H. Broad-beam modeling and experiments for electric spacecraft propulsion. Rev Sci Instrum. 2000;71(2):732–4. https://doi.org/10.1063/1.1150277.
45. Tartz M, Hartmann E, Neumann H. Validated simulation of the ion extraction grid lifetime. Rev Sci Instrum. 2008;79(2):02B905. https://doi.org/10.1063/1.2801376.
46. Eichhorn C, Scholze F, Bundesmann C, Spemann D, Neumann H, Leiter HJ. Two-photon laser-induced fluorescence in a radiofrequency ion thruster plume in krypton. J Propuls Power. 2019;35(6):1175–8. https://doi.org/10.2514/1.b37487.
47. Eichhorn C, Löhle S, Fasoulas S, Leiter H, Fritzsche S, Auweter-Kurtz M. Two-photon laser-induced fluorescence of neutral xenon in a thin xenon plasma. J Propuls Power. 2012;28(5):1116–20. https://doi.org/10.2514/1.B34434.
48. Crofton MW. Measurement of neutral xenon density profile in an ion thruster plume. In: 27th AIAA plasma dynamics and lasers conference. AIAA paper 1996-2290. 1996. https://doi.org/10.2514/6.1996-2290.
49. Crofton MW, Hsu Schouten AG, Young JA, Beiting EJ, Diamant KD. Neutral xenon density in the SPT-140 near-field plume. In: 33rd international electric propulsion conference. Paper IEPC-2013-399. 2013.
50. Williams GJ, Smith TB, Patrick TA, Gallimore AD. Characterization of the FMT-2 discharge cathode plume. In: 26th international electric propulsion conference. Paper IEPC-99-104. 1999.
51. Williams GJ, Smith TB, Gallimore AD. Measurement of 30-centimeter ion thruster discharge cathode erosion. J Propuls Power. 2008;24(5):973–80. https://doi.org/10.2514/1.22982.
52. Cedolin RJ, Hargus WA, Storm PV, Hanson RK, Capelli MA. Laser-induced fluorescence study of a xenon Hall thruster. In: 33rd joint propulsion conference and exhibit. 1997. https://doi.org/10.2514/6.1997-3053.

53. Hargus WA, Capelli MA. Laser-induced fluorescence measurements of velocity within a Hall discharge. Appl Phys B, Lasers Opt. 2001;72(8):961–9. https://doi.org/10.1007/s003400100589.
54. Smith T, Huang W, Reid BM, Gallimore A. Near-field laser-induced fluoresccence velocimetry of neutral xenon in a 6-kW Hall thruster plume. In: 30th international electric propulsion conference. Paper IEPC-2007-229. 2007.
55. Mazouffre S, Gawron D, Sadeghi N. A time-resolved laser induced fluorescence study on the ion velocity distribution function in a Hall thruster after a fast current disruption. Phys Plasmas. 2009;16(4):043504. https://doi.org/10.1063/1.3112704.
56. Spektor R, Diamant KD, Beiting EJ, Raitses Y, Fisch NJ. Laser-induced fluorescence measurements of the cylindrical Hall thruster plume. Phys Plasmas. 2010;17(9):093502. https://doi.org/10.1063/1.3475433.
57. Lejeune A, Bourgeouis G, Mazouffre S. Kr II and Xe II axial velocity distribution functions in a cross-field ion source. Phys Plasmas. 2011;19(76):073501. https://doi.org/10.1063/1.4731688.
58. Huang W, Gallimore A, Smith T. Interior and near-wall ion velocity distribution functions in the H6 Hall thruster. J Propuls Power. 2013;29(5):1146–54. https://doi.org/10.2514/1.b34712.
59. Dancheva Y, Biancalana V, Pagano D, Scortecci F. Measurement of XeI and XeII velocity in the near exit plane of a low-power Hall effect thruster by light induced fluorescence spectroscopy. Rev Sci Instrum. 2013;84(6):065113. https://doi.org/10.1063/1.4811664.
60. MacDonald NA, Capelli MA, Hargus WA. Time-synchronized continuous wave laser-induced fluorescence axial velocity measurements in a diverging cusped field thruster. J Phys D, Appl Phys. 2014;47(11):115204. https://doi.org/10.1088/0022-3727/47/11/115204.
61. Fabris AL, Young CV, Capelli MA. Time-resolved laser-induced fluorescence measurement of ion and neutral dynamics in a Hall thruster during ionization oscillations. J Appl Phys. 2015;118(23):233301. https://doi.org/10.1063/1.4937272.
62. Elias PQ, Jarrige J, Cucchetti E, Packan D. 3D ion velocity distribution function measurement in an electric thruster using laser induced fluorescence tomography. Rev Sci Instrum. 2017;88(11):093511. https://doi.org/10.1063/1.5001304.
63. Svarnas P, Romadanov I, Diallo A, Raitses Y. Laser-induced fluorescence of Xe I and Xe II in ambipolar plasma flow. IEEE Trans Plasma Sci. 2018;46(11):3998–4009. https://doi.org/10.1109/TPS.2018.2857508.
64. Chaplin VH, Jorns BA, Lopez Ortega A, Mikellides IG, Conversano RW, Lobbia RB, Hofer RR. Laser-induced fluorescence measurements of acceleration zone scaling in the 12.5 kW HERMeS Hall thruster. J Appl Phys. 2018;124(18):183302. https://doi.org/10.1063/1.5040388.
65. Bundesmann C, Tartz M, Scholze F, Leiter HJ, Scortecci F, Gnizdor RY, Neumann H. Note: an advanced in situ diagnostic system for characterization of electric propulsion thrusters and ion beam sources. Rev Sci Instrum. 2010;81(4):046106. https://doi.org/10.1063/1.3386585.
66. Bundesmann C, Tartz M, Scholze F, Leiter HJ, Scortecci F, Neumann H. In situ characterization of the accelerator grid of an ion thruster. J Propuls Power. 2011;27(3):532–7. https://doi.org/10.2514/1.50049.
67. Bundesmann C, Eichhorn C, Scholze F, Spemann D, Neumann H, Pagano D, Scaranzin S, Scortecci F, Leiter HJ, Gauter S, Wiese R, Kersten H, Holste K, Köhler P, Klar PJ, Mazouffre S, Blott R, Bulit A, Dannenmayer K. An advanced electric propulsion diagnostic (AEPD) platform for in-situ characterization of electric propulsion thrusters and ion beam sources. Eur Phys J D. 2016;70(10):212. https://doi.org/10.1140/epjd/e2016-70236-0.
68. Pagano D, Scortecci F, Bundesmann C, Eichhorn C, Scholze F, Neumann H, Leiter H, Kersten H, Blott R, Meyer B, Mazouffre S, Bulit A, Gonzales del Amo J. Qualification of the AEPD system as a standard on-ground tool for electric propulsion thrusters. In: 34th international electric propulsion conference. IEPC paper 2015-363. 2015.
69. Scortecci F, Pagano D, Bundesmann C, Eichhorn C, Scholze F, Spemann D, Leiter H, Kersten H, Blott R, Mazouffre S, Klar P, Feili D, Gonzales del Amo J. AEPD system as a standard on-ground tool for electric propulsion thrusters. In: 35th international electric propulsion conference. IEPC paper 2017-33. 2017.
70. Wiese R, Kersten H, Wiese G, Häckel M. Aktive Thermosonde zur Messung des Energieeinstromes. Vak Forsch Prax. 2011;23(3):20–3. https://doi.org/10.1002/vipr.201100461.
71. Wiese R, Kersten H, Wiese G, Bartsch R. Energy influx measurements with an active thermal probe in plasma-technological processes. EPJ Tech Instrum. 2015;2(1):2. https://doi.org/10.1140/epjti/s40485-015-0013-y.
72. Loeb HW. Recent work on radio frequency ion thrusters. J Spacecr Rockets. 1971;8(5):494–500. https://doi.org/10.2514/3.59683.
73. Groh KH, Loeb HW. Radio-frequency ion sources for space propulsion (invited). Rev Sci Instrum. 1992;63(4):2513–8. https://doi.org/10.1063/1.1142875.
74. Zeuner M, Scholze F, Dathe B, Neumann H. Optimisation and characterisation of a TCP type RF broad beam ion source. Surf Coat Technol. 2001;142–144:39–48. https://doi.org/10.1016/S0257-8972(01)01219-1.
75. Bebb HB, Gold A. Multiphoton ionization of hydrogen and rare-gas atoms. Phys Rev. 1966;143(1):1–24. https://doi.org/10.1103/PhysRev.143.1.
76. Bonin KD, McIlrath TJ. Two-photon electric-dipole selection rules. J Opt Soc Am B. 1984;1(1):52–5. https://doi.org/10.1364/JOSAB.1.000052.
77. Niemi K, Schulz-von der Gathen V, Döbele HF. Absolute calibration of atomic density measurements by laser-induced fluorescence spectroscopy with two-photon excitation. J Phys D, Appl Phys. 2001;34(15):2330–5. https://doi.org/10.1088/0022-3727/34/15/312.
78. Goehlich A, Kawetzki T, Döbele HF. On absolute calibration with xenon of laser diagnostic methods based on two-photon absorption. J Chem Phys. 1998;108(22):9362–70. https://doi.org/10.1063/1.476388.
79. Eichhorn C, Scholze F, Bundesmann C, Spemann D, Neumann H, Leiter HJ. Two-photon laser-induced fluorescence diagnostics of a radiofrequency ion thruster: measurements in xenon and krypton. In: 36th international electric propulsion conference. Paper IEPC-2019-503. 2019.
80. Eichhorn C, Scholze F, Bundesmann C, Spemann D, Neumann H, Leiter HJ. Laser-induced fluorescence in the plume of a radiofrequency ion thruster: measurements and excitation schemes. In: AIAA propulsion and energy forum. AIAA paper 2019-4168. 2019. https://doi.org/10.2514/6.2019-4168.
81. Inoue G, Ku JK, Setser DW. Laser induced fluorescence study of Xe($5p^5 6p$, $5p^5 6p'$, $5p^5 7p$, and $5p^5 6d$) states in Ne and Ar: radiative lifetimes and collisional deactivation rate constants. J Chem Phys. 1984;81(12):5760–74. https://doi.org/10.1063/1.447628.

82. Whitehead CA, Pournasr H, Bruce MR, Hong C, Kohel J, Layne WB, Keto JW. Deactivation of two-photon excited Xe($5p^5$6p,6p',7p) and Kr($4p^5$5p) in xenon and krypton. J Chem Phys. 1995;105(5):1965–80. https://doi.org/10.1063/1.468763.
83. Demtröder W. Laser spectroscopy: vol. 1 basic principles. 4th ed. Berlin: Springer; 2008. https://doi.org/10.1007/978-3-540-73418-5.
84. Suzuki M, Katoh K, Nishimiya N. Saturated absorption spectroscopy of Xe using a GaAs semiconductor laser. Spectrochim Acta A. 2002;58(11):2519–31. https://doi.org/10.1016/s1386-1425(02)00069-0.
85. White HE, Elliott H. Introduction to atomic spectra. New York: McGraw-Hill; 1934.
86. Reynolds TW, Richley EA. Thermionic emission from caesium-coated electrostatic ion thruster electrodes. In: Technical report TN D-1879. NASA LeRC: Cleveland; 1963. https://ntrs.nasa.gov/api/citations/19630012010/downloads/19630012010.pdf.
87. Cedolin RJ, Hanson RK, Cappelli MA. Laser-induced fluorescence measurements of resonance broadening in xenon. Phys Rev A. 1996;54(1):335–42. https://doi.org/10.1103/physreva.54.335.
88. Smith TB, Herman DA, Gallimore AD, Drake RP. Deconvolution of axial velocity distributions from Hall thruster LIF spectra. In: 27th international electric propulsion conference. Paper IEPC-01-0019. 2001.
89. Meija J, Coplen TB, Berglund M, Brand WA, de Bièvre P, Gröning M, Holden NE, Irrgeher J, Loss RD, Walczyk T, Prohaska T. Atomic weights of the elements 2013 (IUPAC technical report). Pure Appl Chem. 2016;88(3):265–91. https://doi.org/10.1515/pac-2015-0305.